

DOI: 10.1002/ ((please add manuscript number))

**Article type:** Full paper

**Title: Tailoring carbon nanotube microsphere architectures with controlled porosity**

*Zishuai Zhang, Mohammad Amin Sadeghi, Rhodri Jervis, Siyu Ye, Jeff T. Gostick, Jake E Barralet<sup>‡\*</sup> and Geraldine Merle<sup>‡</sup>*

Z. Zhang, Prof. J. E. Barralet

Faculty of Dentistry, McGill University, Montreal, H3A 2B2, Canada

Email: [jake.barralet@mcgill.ca](mailto:jake.barralet@mcgill.ca)

M.A. Sadeghi

Department of Chemical Engineering, McGill University, Montreal, H3A 2B2, Canada

Dr. R. Jervis

Electrochemical Innovation Lab, University College London, London, WC1E 7JE, UK.

Dr. S. Ye

Ballard Power Systems, 9000 Glenlyon Parkway, Burnaby, V5J 5J8, Canada

Prof. J.T. Gostick

Department of Chemical Engineering, University of Waterloo, Waterloo, N2L 3G1, Canada

Prof. G. Merle

Faculty of Medicine, McGill University, Montreal, H3A 0C5, Canada

**Keywords:** carbon nanotube microspheres, porosity, macropores, oxygen reduction reaction, electrocatalyst

**Abstract:** Nanomaterials are at the core of fuel cell electrodes, providing high area catalytic, proton and electron conducting surfaces, traditionally on carbon black supports. Other carbons (e.g. CNTs and graphene) are less prone to oxidation however their handling is not trivial due to health risks associated to their size. Assembling them into microscale structures without jeopardizing their performance is ideal however there are mass transfer limitations as thickness increases. In this work, we used a soluble acicular calcium carbonate (aragonite) as a porogen to create connected porosity in microspheres. Increasing macroporosity had a considerable positive impact on the mass transfer process. We combined experimental manipulation of porosity of the microspheres with pore network modeling to better understand how pore distribution throughout the whole microsphere could optimize platinum utilization decorated onto the carbon nanotubes. ORR activity was compared with the prepared composite materials and a commercial Pt/C catalyst for 4 weeks. The composite materials exhibited a highly

interconnected network resulting in a 3.4 times higher oxygen reduction reaction activity (at 0.9V vs RHE) than that of the nanoporous spheres with no macroporosity.

## 1. Introduction

Fuel cells have been developed over the past decades as clean alternative energy source due to their high energy efficiency and low pollutant emission properties.<sup>[1-3]</sup> However, issues including low platinum utilization and poor kinetics for oxygen reduction reaction (ORR) limit their adoption.<sup>[4]</sup> To overcome these issues, the majority of efforts were made to synthesize and tailor nanoscale materials due to their high specific surface area and surface energy, which ultimately led to the high catalytic activity.<sup>[5-6]</sup> Carbon nanotubes (CNTs) have high surface areas and excellent electrical conductivity and resistance to corrosion, however, industrial are still reluctant to manufacture with nanosized carbons that are associated with health hazards.<sup>[7]</sup> Moving from the nano- to micro-scale through assembly without compromising the nanomaterial properties, can improve handling, nevertheless, mass transfer of reactants/products and ion diffusion process can be strongly retarded by small pore sizes (<2 nm) introduced through the assembly process.<sup>[8]</sup> Recent studies have shown that the diffusion coefficients of ions significantly decreases by orders of magnitude in nanochannels compared with bulk values, which may be attributed to the surface charge in narrow-size pores.<sup>[9]</sup> Porosity can be introduced into catalytic materials through several techniques including: solvent evaporation, polymerization, seed swelling, spray drying, synthesis and phase separation methods etc.<sup>[10-14]</sup> Generally, many experimental results have shown increased porosity facilitates the mass transport and ion diffusion processes, thus helping electrochemical reactions to occur.<sup>[15-18]</sup>

Our group has previously developed a cavitation mediated assembly method that produced 3D microstructured architectures from several materials including nano-carbon.<sup>[7, 19]</sup> The prepared

microspheres generally only with nanopores. Studies on the effect of porosity on electroactivity performances reported that accessible meso- and macropores enhanced ORR catalytic activity by facilitating mass transport of the species towards and away from active sites.<sup>[1, 20-21]</sup> In this manuscript, we study the impact of macro-porosity on carbon nanotube microsphere (CN $\mu$ S) supported Pt(Fe) nanoparticles towards ORR activity and durability.

We successfully applied our cavitation induced assembly method to introduce porogens into the 3D microstructured architectures. This was carried out by simply adding porogen in the starting mixture before the assembly process and then dissolving in acid. CN $\mu$ S with increased porosity were prepared by varying the ratio of porogen: CNT. Finally, Pt and PtFe nanoparticles were deposited on the selected CN $\mu$ S. It has previously been demonstrated that alloying Pt with transition metals such as Co<sup>[22-24]</sup>, Pd<sup>[25-27]</sup>, Cu<sup>[23, 28]</sup> and Fe<sup>[29-30]</sup> can positively affect the Pt structure, enhancing both catalytic activity and durability.<sup>[29]</sup> Of particular interest, PtFe nanoparticles have been proven to be highly active for ORR and less susceptible to dissolution in acidic conditions due to the change of both geometric and electronic structures of Pt, furthermore, the central position of Pt around Fe atoms maximizes its utilization.<sup>[31-32]</sup> Here, we report that PtFe nanoparticles supported on CN $\mu$ S could have very good ORR performance at the appropriate macroporosity level (50.3 mA/mg<sub>Pt</sub> at 0.9 V vs RHE; ~10% electrochemical surface area (ECSA) loss after 4 weeks) compared to the commercial Pt/C catalyst (47.0 mA/mg<sub>Pt</sub> at 0.9 V vs RHE; ~70% ECSA loss after 4 weeks).

## 2. Results and Discussion

### 2.1 Structure, morphology and characterization

Aragonite rods were prepared by calcium carbonate precipitation in urea.<sup>[33]</sup> They exhibited a smooth surface, an average length of 800 nm and a diameter of 100 nm (**Figure 1a**). Oxidized

nano-carbon can be assembled into larger spheres upon ultrasound.<sup>[7]</sup> The porogen was mixed with the phosphate treated oxidized carbon nanotubes in different ratios from 10 to 40 (wt.%,  $W_{\text{aragonite}}/W_{\text{CN}\mu\text{S}}$ ), and assembled by one-hour sonication (**microspheres disintegrated when aragonite was over 40 wt.%**). **Figure 1b** reveals the distribution of aragonite within the microspheres. Removal of the aragonite **was** achieved by storage in 1M HCl solution for 10 minutes. In addition, to the rod-like pores generated by the aragonite, some holes and cracks appeared on the microsphere likely caused by the CO<sub>2</sub> bubbles produced during the porogen removal process (**Figure 1c**). **Figure 1d** is an illustration of the microspheres with and without macroporosity, suggesting microspheres with macroporosity facilitating the oxygen diffusion process.

Thermogravimetric analysis (TGA) combined with X-ray powder diffraction (XRD) analysis were carried out to determine the amount of aragonite in CN $\mu$ S (**Figure 2**). The XRD pattern after TGA (800 °C, **air**) showed the thermal decomposition from aragonite to calcium oxide (CaO), from which the loading of original porogen (wt.%) within CN $\mu$ S can be determined ( $\text{CaCO}_3 \rightarrow \text{CaO} + \text{CO}_2$ ). The results showed that the amount of aragonite assembled with CNTs gradually increased with the increasing of the initial aragonite amount (Figure 2b). **Figure S1** shows photographs of the microspheres after mechanical shaking, and the clear supernatant indicates few CNTs detaching from CN $\mu$ S during the mechanical shaking, illustrating the microsphere stability.

The morphology of CN $\mu$ S with acicular porogen was investigated by scanning electron microscopy (SEM) (**Figure 3**). Aragonite appeared well-dispersed on the surface of CN $\mu$ S up to a loading of 30 wt.%, whereas at concentration of 40 wt.%, aragonite tended to agglomerate. After removing porogen, CN $\mu$ S exhibited a rough surface, porous structure with more large voids as the wt.% of aragonite increased. The interior structure of these CN $\mu$ S was studied by focused ion beam (FIB) SEM (**Figure 4**). The cross-section of the CN $\mu$ S without aragonite exhibited a compacted inner core structure with nanopores, whereas interconnected

pores were present inside the CN $\mu$ S with 40wt% loading. The aragonite was distributed through the whole microsphere, confirming the porogen was not confined to the microsphere surface. Tomography images of CN $\mu$ S (40%, with/ without porogen) and CN $\mu$ S (0%) samples were scanned by a micro-CT (Figure 4). It clearly showed that the porogen is not homogeneously distributed through the whole microsphere, which further confirmed by the images of CN $\mu$ S (40%) with a cluster of macropores presenting after the porogen removal. No obvious macropores had been detected for porogen-free control CN $\mu$ S (0%) which validated the results of porogen.

The porous CN $\mu$ S densities were calculated using Stokes' law by measuring the settling times of various CN $\mu$ S traveling a fixed distance in ethanol (**Table S1**), and the results confirmed the decreasing bulk densities (increasing porosity) of microspheres were synthesized as porogen was added (**Figure S2**).

To further investigate the porosity of CN $\mu$ S (40%) and CN $\mu$ S (0%), nitrogen adsorption-desorption analysis was conducted (**Figure S3**). At the initial adsorption stage (i.e.,  $P/P_0 < 0.1$ ), both samples had a sharp adsorption of nitrogen, indicating the existence of nanopores.<sup>[34-35]</sup> They also exhibited similar hysteresis loops for mesopores at  $P/P_0 > 0.4$  stage, indicating the disordered pore network inside the porous matrix.<sup>[36-37]</sup> The pore size distribution (PSD) of the two samples indicated a bimodal micropore size distribution about 1.5 nm and 3.0 nm (Figure S3 b). The BET surface area for the microspheres prepared with and without porogen remained unchanged ( $328$  and  $323 \text{ m}^2 \text{ g}^{-1}$  for CN $\mu$ S (40%) and CN $\mu$ S (0%), respectively).

Pt and PtFe nanoparticles were deposited via chemical reduction, and ethylene glycol was added as capping agent in the reduction to control Pt reduction and nucleation.<sup>[38]</sup> **Figures 5a, b** show well-dispersed and uniform Pt nanoparticles with an average size of  $2.36 \pm 0.08$  nm ( $N=70$ ). High-resolution transmission electron microscope (HRTEM) confirmed a  $d$  spacing of about 0.23 nm, corresponding to (111) facet of Pt (Insert Figure 5b), corroborating the

XRD result (Figure 5f). PtFe particles were relatively larger (average size  $3.61 \pm 0.10$  nm), and less dispersed than Pt nanoparticles with many clusters apparent (Figure 5c, d). The high-temperature annealing to convert the disordered face-centered cubic (fcc) structure to the more stable and active face-centered tetragonal (fct) structure caused slight coalescence of neighbouring nanoparticles.<sup>[31-32]</sup> A  $d$  spacing of 0.18 nm and 0.22 nm corresponding to (200) and (111) facets respectively were measured (Insert Figure 5d). TEM elemental mapping of Pt and Fe and high-angle annular dark field-scanning transmission electrons microscope (HAADF-STEM) images of the nanoparticles overlapped and confirmed the presence of Pt and Fe (atomic ratio 3:2) (Figure 5g, h, **Table S2**). **The initial mole ratio of Pt to Fe was set as 1:1 based on the previous results reported by Du et al. for a highly active ORR PtFe nanoalloy.**<sup>[39]</sup> The crystal structure of the particles was analyzed by XRD in Figure 5f, showing a shift to a larger angle ( $2\theta=41.5^\circ$ ) for PtFe (111) facet compared to Pt ( $2\theta=40.5^\circ$ ), suggesting a slight contraction of the lattice which has been reported due to incorporation of the smaller iron atom in the PtFe alloy.<sup>[29]</sup> The high-resolution x-ray photoelectron spectroscopy (XPS) further confirmed the presence of Pt and Fe atoms on the PtFe/CN $\mu$ S(40%) (**Figure S4**).

## 2.2 Electrochemical characterization

Electrochemical activities of the Pt(Fe)/CN $\mu$ S catalysts for ORR were assessed towards ORR in acidic conditions (0.1M HClO<sub>4</sub>). The catalytic inks were prepared, drop-cast and dried on glassy carbon rotating disk electrodes (RDE). All the measurements were carried out in 0.1M HClO<sub>4</sub> solution at room temperature (25 °C) with the same loading of Pt amount (0.04 mg cm<sup>-2</sup>).

Cyclic voltammetry (CV) of **electrocatalysts formed by Pt and PtFe supported CN $\mu$ S** electrocatalysts prepared with different aragonite loadings ranging from 0 to 40 wt. % were performed. As expected, results showed that the porosity did not have a significant effect on

ECSA of Pt nanoparticles (**Figure 6a**), and Pt supported CN $\mu$ S electrocatalysts exhibited a narrow ECSA ranging from 50-60 m<sup>2</sup>/g<sub>Pt</sub> whereas an ECSA of 67 m<sup>2</sup>/g<sub>Pt</sub> has been achieved for PtFe/CN $\mu$ S catalysts (**Table S3**). The slightly increased ECSA is attributed to higher Pt atoms utilization in the alloy than pristine Pt particles.<sup>[40-41]</sup> To investigate the ORR activity, linear scan voltammetry (LSV) tests were carried out (Figure 6b). The results showed that increasing the amount of porogen (i.e. porosity) caused a shift of the onset potentials: the onset potential of CN $\mu$ S (40%) was 50 mV higher than CN $\mu$ S (0%) for Pt based catalysts. Additionally, the limiting currents were also increased with the incremental increase of porosity (e.g. 5.7 mA cm<sup>-2</sup> for CN $\mu$ S (40%) and 4.6 mA cm<sup>-2</sup> for CN $\mu$ S (0%)). These results suggested that macroporosity improved ORR activity certainly through enhanced dissolved oxygen diffusion and ion diffusion processes within microspheres. PtFe/CN $\mu$ S(40%) had an enhanced ORR activity ( $\approx$ 3.18 times higher of mass activity at 0.9 V) compared to Pt/CN $\mu$ S(40%), which has been attributed to geometric lattice structure effects and higher Pt utilization (Figure 6c).<sup>[40]</sup>

The most common benchmarks used to evaluate ORR catalytic activity are specific and mass activities at 0.9 V versus RHE. Kinetic current density ( $I_k$ ), determined from LSV curves and the Koutecky-Levich (K-L) equation, is further used to calculate specific and mass activities.<sup>[42]</sup>

$$\frac{1}{I} = \frac{1}{I_k} + \frac{1}{I_d} \quad (1)$$

Where  $I$  is experimental current density and  $I_d$  is limiting current density. Based on **Equation 1**, either a higher measured current or a lower limiting current will lead to a higher kinetic current. Figure 6e shows PtFe/CN $\mu$ S (40%) had the highest kinetic current density (at 0.9V) when the Pt loading was 0.04 mg cm<sup>-2</sup>, which was comparable to commercial Pt/C. **The high**

catalytic activity of PtFe/CN $\mu$ S (40%) is due to 1) highly active PtFe catalytic sites, 2) high surface area of the CNT supports and 3) interconnected porosity inside microspheres facilitating oxygen diffusion process. According to the kinetic currents and ECSA values, mass and specific activities were ordered in similar sequence inferring that increasing percentage of porogen led to a better activity (Figure 6c). These results corroborate that the increasing porosity results in an enhanced ORR activity, and PtFe particles with fct structure had a higher ORR activity than Pt alone. Note that, Pt/CN $\mu$ S (40%) had 3.4 times higher mass activity than Pt/CN $\mu$ S (0%).

Tafel plots were used to investigate the electrocatalytic activity and reaction mechanism (Figure 6d).<sup>[43]</sup> In the low current density (lcd) region, the slope of 60 mV dec<sup>-1</sup> is theoretically expected.<sup>[43]</sup> The results show the slopes for PtFe/CN $\mu$ S(40%), Pt/CN $\mu$ S(40%) and commercial Pt/C are 68.5, 76.7 and 71.5 mV dec<sup>-1</sup>, indicating a higher electron transfer coefficient for adsorbed oxygen species for PtFe based catalyst than the Pt based catalysts.<sup>[44]</sup>

Chronoamperometry measurements at 0.6V (vs. RHE) were performed on PtFe/CN $\mu$ S (40%), Pt/CN $\mu$ S (40%) and commercial Pt/C electrodes to assess their durability in acidic media (Figure 6e). After 20,000s, the commercial Pt/C catalyst retained 80% of initial current density, and PtFe/CN $\mu$ S (40%) retained 84% initial current density. Pt/CN $\mu$ S (40%) only retained 60%. This is in agreement with J. Kim et al. reported excellent anti-dissolution properties of PtFe in acidic conditions.<sup>[32]</sup> To further evaluate the catalyst ORR performance, corrosion tests were conducted in acidic media (0.1M HClO<sub>4</sub>). ECSA is an indicator reflecting catalysts active sites for electrochemical reactions, and its value is significant for evaluating Pt(Fe) particle corrosion resistant property (**Figure 7**). ECSA values dropped sharply from 100% to around 35% after 15 days for commercial Pt/C, and Pt/CN $\mu$ S (40%), PtFe/CN $\mu$ S (40%) with around 57% and 85% retained, respectively. Furthermore, Pt/C lost around 70% of ECSA after 4 weeks, whereas Pt/CN $\mu$ S (40%) stabilised after 2 weeks at 60%. PtFe/CN $\mu$ S

(40%) outperformed both Pt/CN $\mu$ S and commercial Pt/C for corrosion resistance and showed ~10% loss over the 4-week due to its excellent anti-dissolution ability. **Note that, the ECSA at Day 4 and 22 showed unusual drops in PtFe/CN $\mu$ S (40%), which may be caused by measurement errors (affected by measurement conditions).**

## 2.2 Pore-network Modeling

We conducted numerical simulation studies to consider the problem of reaction-diffusion in a single hierarchically porous agglomerate particle comprised of nanopores and macropores. There are two different paradigms for modeling transport in porous media namely volume-averaged continuum or briefly continuum models, and pore-scale models.<sup>[45]</sup> In the former, it is assumed that a representative volume element that encapsulates the microstructural features of the domain exists. Therefore, the governing mass transport equations are written and solved for the porous domain altogether as a single homogeneous entity, disregarding the microstructure of the porous material.<sup>[46]</sup> One direct necessity of this methodology is that effective properties such as effective diffusivity are input parameters and therefore must be either measured experimentally or calculated theoretically. In the latter, the true geometry of the porous material, i.e. an intricate interconnected network of void and solid, is considered for which the governing equations are solved.

In this study, we employ pore network modeling, to capture the effects of microstructure, i.e. hierarchical porosity, on the catalytic performance of the agglomerate. In this method, the porous material is approximated by an equivalent graph of nodes, with each node representing a void volume within the actual porous domain, enclosed by the solid phase. This simplification reduces the computational complexity of the resulting system of equations by 4-5 orders of magnitude and therefore, allows for simulating the whole particle agglomerate in a reasonable time (~ few hours) that otherwise is not possible.<sup>[47]</sup>

**Figure 8** shows four pore network models in 2D representing hierarchically porous nanoparticles at four different macroporosity created using a procedure explained in section 4.3. A constant concentration boundary condition  $c_A = 1 \text{ mol/m}^3$  was applied to the outermost layer of the agglomerate particle. The simulations were carried out under steady-state assumption. **Figure 9** shows the concentration profile within the agglomerate particle at four different macroporosities obtained from the pore network simulation. Note that in all four scenarios, due to poor mass transport, a starvation region is apparent at the core of the particle. According to **Figure 9**, however, the size of this region is shrinking as macroporosity is increased. As more microporosity was created, although the theoretically available reaction area was decreased, the resulting boost in mass transport due to creation of the ‘diffusion-highways’ outweighed this compromise. It is worth mentioning that such a mechanism became even more pronounced when the size distribution of the nanopores shifted towards smaller pore sizes. This phenomenon occurs since as the pore size approached the mean free path of the diffusing species, mass transport tended to become limited by Knudsen diffusion, because of frequent collisions of molecules with pore walls.

The higher rate of ORR seen at higher macroporosity could be attributed to two distinct sources. First, regardless of which diffusion regime was dominating the overall mass transport, as the species diffused and reacted through the agglomerate particle, the concentration dropped, which led to starvation of its core. Macropores act as intermediaries between the starved core of the agglomerate and its ambient, mitigating the concentration drop. Second, the mass transport in some of the nanopores was limited by the Knudsen diffusion due to their relatively small size. This limitation caused the concentration of species to undergo an even a more rapid drop as they diffused through the agglomerate towards its core. Note that the former is because of the presence of the macroscopic length scale of the problem, and therefore can be characterized by the diameter of the agglomerate particle, while

the latter is due to the presence of the microscopic length scale, and thus can be characterized by the diameter of the nanopores.

The pore network simulation results presented here confirm the practicality of using porogens for creating hierarchical porous structures with high catalytic activity. These results are applicable to similar systems given that the reaction kinetics, the average agglomerate size, and the size distribution of the nanopores are in a similar range. Whether creating such hierarchically porous structures is always advantageous strongly depends on these parameters. Therefore, such simulations can be used as a guideline for determining the optimal amount of porogen for achieving maximum catalytic activity for any catalyst system of an arbitrary size, given that the reaction kinetics is reasonably understood.

### **3. Conclusion**

In summary, we successfully produced different porous CN $\mu$ S by simple, and fast ultrasonic method incorporating aragonite as soluble acicular porogen during the assembly. Removal of the porogen created hierarchically porous CN $\mu$ S that enabled study and insight of the relationship between macroporosity and ORR activity. In addition, PtFe alloying improved Pt utilization and decreased its acid dissolution. To gain a better understanding, we conducted pore network modeling simulations showing that starvation volume at the core of microspheres is shrinking with macroporosity increasing. Together, our studies demonstrate that tailored porosity in the 3D structure is essential for optimizing microspheres' electrochemical catalytic activity.

### **4. Experimental Section:**

#### **4.1 Preparation of Pt(Fe)/ various porosity carbon nanotube microsphere (CN $\mu$ S-x) substrate**

#### 4.1.1 Porous carbon nanotube microsphere (CN $\mu$ S-x) synthesis

Acicular aragonite synthesis process has been reported by *Chen et al.*<sup>[33]</sup> Briefly, 2.45 g calcium acetate (Fisher scientific, lab grade, monohydrate) and 2.25 g urea (Sigma-Aldrich, >99%) were dissolved into 50 mL deionized water under vigorous stirring. 15 mL ethanol was added afterwards. The mixed solution was then heated in a 100 mL air-tight flask at 90 °C for 24 hours with stirring. After the reaction complete, the white precipitation was washed with a large volume of deionized water. Finally, the aragonite was dried in an oven at 50 °C for another 24 hours until it was totally dried.

Carbon nanotubes (CNTs) were oxidized before use: 500 mg multiwall CNTs (Sigma-Aldrich, O.D×L: 6-9 nm ×5  $\mu$ m) were mixed with 100 mL solution of 8.0 M of H<sub>2</sub>SO<sub>4</sub> and 8.0 M of HNO<sub>3</sub> (v/v=3:1, fisher scientific) then sonicated for 2 hours.<sup>[48]</sup> After sonication, oxidized CNTs were rinsed with a large amount of deionized water until pH went back to neutral. Dried the final product in an oven at 40°C for 24 hours for the further use. Various porous CN $\mu$ S were synthesized by removing aragonite from the composite microspheres. A facile and scalable ultrasonic self-assemble approach reported by our lab was applied here to fabricate robust microspheres.<sup>[49]</sup> 20 mg oxidized CNTs were sonicated for one hour in isopropyl alcohol (IPA, Fisher scientific) using an ultrasonic bath (Bransonic 1800, Branson), then mixed with different weight percentages of aragonite (x=0%, 10%, 20%, 30% and 40%;  $w_{\text{aragonite}}/w_{\text{CN}\mu\text{S}}$ ). The mixture was sonicated for another 30 mins, then dried overnight in a vacuum oven. Once dried, the powder was broken into smaller pieces using a metal spatula and weighted. The Na<sub>3</sub>PO<sub>4</sub> solution (90 mM, 40(1+x)  $\mu$ L) was added to the powder then dried in a vacuum oven at 100°C to form xerogel. The produced xerogel was sonicated in 10 mL IPA for 60 min and sieved to get 30-200  $\mu$ m microspheres. 1 M HCl (fisher scientific) was used to remove aragonite embedded in these microspheres. After 10 min stirring in HCl, microspheres were filtered and washed with a large amount of water. Finally, the porous microspheres were dried in a vacuum oven at 40 °C for 24 hours.

#### 4.1.2 Pt nanoparticle deposition

The deposition of Pt nanoparticles was carried out by a chemical reduction method reported by Xie's group.<sup>[50]</sup> First, CN $\mu$ S were sonicated in an aqueous ethylene glycol (EG) solution (fisher scientific,  $v_{\text{water}}/v_{\text{EG}}=2/3$ ) for 30 mins, followed by addition of H<sub>2</sub>PtCl<sub>6</sub>·xH<sub>2</sub>O (Sigma-Aldrich,  $\geq 99.9\%$  trace metal basis) under vigorous stirring. After reflux at 140 °C for 6 hours, the final product was washed by deionized water for several times and then collected. The black powder was dried at 80 °C overnight afterwards.

#### 4.1.3 PtFe nanoparticle deposition

The deposition of alloy PtFe nanoparticles was performed in a similar chemical reduction method in EG solution. CN $\mu$ S were sonicated for 30 min to achieve a well-disperse status in an aqueous ethylene glycol (EG) solution (fisher scientific,  $v_{\text{water}}/v_{\text{EG}}=2/3$ ) Then a mixture of H<sub>2</sub>PtCl<sub>6</sub>·xH<sub>2</sub>O and FeCl<sub>3</sub> (mole ratio 1:1) was added under vigorous stirring. Refluxing the solution at 140 °C for 6 hours, then washed it with deionized water for several times and collected it by centrifugation. After drying the sample overnight, calcined the sample to 800 °C under N<sub>2</sub> atmosphere to form alloy nanoparticles. The product was collected for further use.

## 4.2 Characterization

The morphology of different samples was investigated by scanning electron microscopy (SEM) FEG Quanta Scanning Electron Microscope (Inspect F50, FEI Company, Hillsboro, OR, USA) and Transmission Electron Microscopy (TEM) (Philips CM200) with an electron accelerating voltage of 200 kV and equipped with an energy-dispersive X-ray spectroscopy (EDX) unit. The particles size distribution was obtained by randomly measuring more than 100 nanoparticles in TEM images. Thermogravimetric analysis (TGA) of CN $\mu$ S-x and aragonite was performed by a DSC-TGA instrument (SDT Q600) with the heating rate of

5 °C min<sup>-1</sup>. The CN<sub>μ</sub>S-x samples' nitrogen sorption isotherms were measured via Quantachrome autosorb-1 instrument. The surface area was calculated by Brunauer–Emmett–Teller (BET) method. X-ray diffraction (XRD) patterns were obtained on Bruker D8 Discovery instrument operating at 40 kV and 20 mA, using CuK $\alpha$  radiation. The surface elemental composition of PtFe/CN<sub>μ</sub>S and the atomic bonding information were detected with XPS (Thermo Scientific K-Alpha). The tomography imaging of CN<sub>μ</sub>S was conducted using a Zeiss Xradia Versa 520 micro-CT instrument (Carl Zeiss XRM, Pleasanton, CA) in phase contrast mode. The images with porogen were imaged in absorption contrast mode.

Electrochemical measurements were tested in a three-electrode system: glassy carbon rotating disc electrode (RDE) (0.196 cm<sup>2</sup>), saturated calomel electrode (SCE) and platinum wire work as working electrode, reference electrode and counter electrode respectively. Electrochemical experiments were performed using potentiostat/galvanostat system (VersaSTAT 4, Princeton Applied Research, Oak Ridge, TN). All experiments were tested at the room temperature.

Prior to tests, glassy carbon electrode was polished by 0.05  $\mu$ m alumina oxide suspension and rinsed with deionized water. Cyclic voltammetry (CV) scanned in N<sub>2</sub>-saturated 0.1M HClO<sub>4</sub> solution with the scan range from 0.05V to 1.1V (vs RHE) at 100 mV/s. Linear scan voltammetry (LSV) was performed in O<sub>2</sub>-saturated 0.1 M HClO<sub>4</sub> solution with the scan range from 0.05 V to 1.1 V (vs RHE) at 10 mV/s. The durability tests were performed through chronoamperometry method: a constant potential of 0.6 V (vs RHE). For corrosion resistance test, electrodes were immersed into 0.1M HClO<sub>4</sub> solution all the time and their electrochemical active surface area (ECSA) were tested regularly within one month.

### 4.3 Pore network modeling

For creating the hierarchy of porosity, we followed the procedure developed by Sadeghi et al.<sup>[51]</sup> We started by a porous network that is only consisted of nanopores. Afterwards, a

randomly-picked nanopore with its neighboring pores up to a cut-off radius are replaced with a single macropore. This process is consecutively repeated until the desired macroporosity is achieved. Macroporosity  $\phi_m$  is defined as the volume fraction of macropores measured with respect to the total volume of the particle. We used the open-source software OpenPNM for generating the hierarchical networks as well as for solving the diffusion reaction algorithm on the generated structures.<sup>[52]</sup>

To obtain the concentration profile within the network model of the particle, a material balance is written around each pore, as defined by Eq. (2), which leads to a linear system of equations that needs to be solved.

$$-\sum_{k=1}^{N_i} m_{ik} S_{ik} + R_i = 0 \quad i = 1, 2, \dots, N_p \quad (2)$$

Here,  $m_{ik}$  is the diffusive mass flux between pores  $i$  and  $k$ , and  $S_{ik}$  is the cross-section area of the throat connecting these two pores,  $N_i$  is the number of adjacent pores to pore  $i$ , and finally  $R_i$  is the net reaction rate at pore  $i$  <sup>[51, 53]</sup>. For simplicity, electrochemistry was ignored, and the reaction was assumed to be of first order. Since the surface area of the nanopores is much higher than that of the macropores, the reaction was assumed to only occur in nanopores. Furthermore, the assumption of first order kinetics eliminates the nonlinearity in the ORR rate equation, while preserving the qualitative behavior of the system. The justification of this statement is explained in the following. Note that the ORR rate equation reads as follows

$$r = j_0 A \left( \frac{c_{O_2}}{c_{O_2}^*} \right) \exp \left( -\frac{\alpha_c z}{RT} \eta \right) \quad (3)$$

where  $j_0$  is the exchange current density,  $A$  is the reaction surface area,  $c$  is the concentration of oxygen near the reaction site,  $c_{O_2}^*$  is the reference concentration of oxygen,  $\alpha_c$  is the cathodic transfer number,  $z$  is the number of electrons involved in the ORR,  $R$  is the universal gas constant,  $T$  is temperature, and finally  $\eta$  is the activation overpotential. Eq. 2 can be

rearranged such to be considered first order with respect to the concentration of oxygen as  $r = k_a c_{O_2}$  where  $k_a$  is a nonlinear rate constant as defined below.

$$k_a = \frac{j_0 A}{c_{ref}} \exp\left(-\frac{\alpha_c z}{RT} \eta\right) \quad (4)$$

The concentration of oxygen is maximum at the surface of the particle and continually drops toward its core because of mass transfer resistances, decreasing the rate of ORR. Likewise, because of the ohmic resistances, the voltage of the conducting phase, and consequently the magnitude of the activation overpotential  $|\eta|$ , both monotonically decrease when moving toward the core of the particle. Therefore, since  $\exp(x)$  is a monotonic function, the nonlinear rate constant,  $k_a$ , also decreases when approaching the core of the agglomerate particle. Thus, employing a nonlinear rate constant, compared to a fixed one, merely slows down the depletion rate of oxygen, and therefore, does not change any qualitative trend.

### References:

- [1] G. A. Ferrero, K. Preuss, A. B. Fuertes, M. Sevilla, M. M. Titirici, *J. Mater. Chem. A* **2016**, *4*, 2581.
- [2] Z. Zhang, J. H. Lopes, S. Ye, J. T. Gostick, J. E. Barralet, G. Merle, *J. Electrochem. Soc.* **2016**, *163*, D615.
- [3] Z. Zhang, M. Ye, E. J. Harvey, G. Merle, **2019**, *166*, H135.
- [4] Y. Bing, H. Liu, L. Zhang, D. Ghosh, J. Zhang, *Chem. Soc. Rev.* **2010**, *39*, 2184.
- [5] H. Lv, D. Li, D. Strmcnik, A. P. Paulikas, N. M. Markovic, V. R. Stamenkovic, *Nano Energy* **2016**, *29*, 149.
- [6] N. Sharma, H. Ojha, A. Bharadwaj, D. P. Pathak, R. K. Sharma, *RSC Advances* **2015**, *5*, 53381.
- [7] Z. Zhang, S. Ye, U. Gbureck, J. E. Barralet, G. Merle, **2018**, *28*, 1706832.
- [8] O.-H. Kim, Y.-H. Cho, S. H. Kang, H.-Y. Park, M. Kim, J. W. Lim, D. Y. Chung, M. J. Lee, H. Choe, Y.-E. Sung, *Nat Commun* **2013**, *4*, 2473.
- [9] J. Wang, L. Zhang, J. Xue, G. Hu, *Biomicrofluidics* **2014**, *8*, 024118/1.
- [10] Y. Cheng, H. Lu, K. Zhang, F. Yang, W. Dai, C. Liu, H. Dong, X. Zhang, *Carbon* **2018**, *128*, 38.
- [11] H. Yang, F. Hu, Y. Zhang, L. Shi, Q. Wang, *Nano Res.* **2016**, *9*, 207.
- [12] S. Marzorati, J. M. Vasconcelos, J. Ding, M. Longhi, P. E. Colavita, *J. Mater. Chem. A* **2015**, *3*, 18920.
- [13] L. Jiang, Y. Zhao, J. Zhai, *Angew. Chem., Int. Ed.* **2004**, *43*, 4338.
- [14] Y. Cai, Y. Chen, X. Hong, Z. Liu, W. Yuan, *Int. J. Nanomed.* **2012**, *8*, 1111.
- [15] I. Kone, A. Xie, Y. Tang, Y. Chen, J. Liu, Y. Chen, Y. Sun, X. Yang, P. Wan, *ACS Appl. Mater. Interfaces* **2017**, *9*, 20963.
- [16] S. J. Ha, J. H. Moon, *Journal of Physical Chemistry C* **2017**, *121*, 12046.
- [17] G. J. Yang, C. J. Li, S. Q. Fan, J. C. Gao, *Surface & Coatings Technology* **2011**, *205*, 3205.
- [18] Z. Yu, R. N. Carter, J. Zhang, *Fuel Cells* **2012**, *12*, 557.
- [19] A. Fraser, Z. Zhang, G. Merle, U. Gbureck, S. Ye, J. Gostick, J. Barralet, **2018**, *28*, 1803713.

- [20] J. Liang, Y. Zheng, J. Chen, J. Liu, D. Hulicova-Jurcakova, M. Jaroniec, S. Z. Qiao, *Angew. Chem., Int. Ed.* **2012**, *51*, 3892.
- [21] M. Xiao, J. Zhu, L. Feng, C. Liu, W. Xing, *Adv. Mater. (Weinheim, Ger.)* **2015**, *27*, 2521.
- [22] R. Loukrakpam, J. Luo, T. He, Y. Chen, Z. Xu, P. N. Njoki, B. N. Wanjala, B. Fang, D. Mott, J. Yin, J. Klar, B. Powell, C.-J. Zhong, *J. Phys. Chem. C* **2011**, *115*, 1682.
- [23] M. Oezaslan, P. Strasser, *J. Power Sources* **2011**, *196*, 5240.
- [24] N. Travitsky, T. Ripenbein, D. Golodnitsky, Y. Rosenberg, L. Burshtein, E. Peled, *J. Power Sources* **2006**, *161*, 782.
- [25] S. M. Alia, K. O. Jensen, B. S. Pivovar, Y. Yan, *ACS Catal.* **2012**, *2*, 858.
- [26] X. Li, S. Park, B. N. Popov, *J. Power Sources* **2010**, *195*, 445.
- [27] H. Ye, R. M. Crooks, *J. Am. Chem. Soc.* **2007**, *129*, 3627.
- [28] I. Dutta, M. K. Carpenter, M. P. Balogh, J. M. Ziegelbauer, T. E. Moylan, M. H. Atwan, N. P. Irish, *J. Phys. Chem. C* **2010**, *114*, 16309.
- [29] X. X. Du, Y. He, X. X. Wang, J. N. Wang, *Energy Environ. Sci.* **2016**, *9*, 2623.
- [30] A. R. Malheiro, J. Perez, H. M. Villullas, *J. Electrochem. Soc.* **2009**, *156*, B51.
- [31] D. Y. Chung, S. W. Jun, G. Yoon, S. G. Kwon, D. Y. Shin, P. Seo, J. M. Yoo, H. Shin, Y.-H. Chung, H. Kim, B. S. Mun, K.-S. Lee, N.-S. Lee, S. J. Yoo, D.-H. Lim, K. Kang, Y.-E. Sung, T. Hyeon, *J. Am. Chem. Soc.* **2015**, *137*, 15478.
- [32] J. Kim, Y. Lee, S. Sun, *J. Am. Chem. Soc.* **2010**, *132*, 4996.
- [33] S.-F. Chen, S.-H. Yu, J. Jiang, F. Li, Y. Liu, *Chem. Mater.* **2006**, *18*, 115.
- [34] K. Qiu, G. Chai, C. Jiang, M. Ling, J. Tang, Z. Guo, *ACS Catal.* **2016**, *6*, 3558.
- [35] M. Thommes, *Chem. Ing. Tech.* **2010**, *82*, 1059.
- [36] L. H. Cohan, *J. Am. Chem. Soc.* **1938**, *60*, 433.
- [37] D. H. Everett, F. W. Smith, *Trans. Faraday Soc.* **1954**, *50*, 187.
- [38] N. Steinfeldt, *Langmuir* **2012**, *28*, 13072.
- [39] X. X. Du, Y. He, X. X. Wang, J. N. Wang, *Energy & Environmental Science* **2016**, *9*, 2623.
- [40] P. Strasser, *Acc. Chem. Res.* **2016**, *49*, 2658.
- [41] L. Chen, L. Kuai, B. Geng, *CrystEngComm* **2013**, *15*, 2133.
- [42] K. Gong, F. Du, Z. Xia, M. Durstock, L. Dai, *Science (Washington, DC, U. S.)* **2009**, *323*, 760.
- [43] T. Shinagawa, A. T. Garcia-Esparza, K. Takanabe, *Sci Rep* **2015**, *5*, 13801.
- [44] A. Muthukrishnan, Y. Nabae, C. W. Chang, T. Okajima, T. Ohsaka, *Catal. Sci. Technol.* **2015**, *5*, 1764.
- [45] M. Sahimi, Editor, *Flow and Transport in Porous Media and Fractured Rock: From Classical Methods to Modern Approaches, Second Edition*, Wiley-VCH, **2011**.
- [46] R. Hill, *Journal of the Mechanics and Physics of Solids* **1963**, *11*, 357.
- [47] H. J. Vogel, J. Tolke, V. P. Schulz, M. Krafczyk, K. Roth, *Vadose Zone Journal* **2005**, *4*, 380.
- [48] Y. Xing, L. Li, C. C. Chusuei, R. V. Hull, *Langmuir* **2005**, *21*, 4185.
- [49] D. C. Bassett, G. Merle, B. Lennox, R. Rabiei, F. Barthelat, L. M. Grover, J. E. Barralet, *Adv. Mater. (Weinheim, Ger.)* **2013**, *25*, 5953.
- [50] Z.-F. Li, L. Xin, F. Yang, Y. Liu, Y. Liu, H. Zhang, L. Stanciu, J. Xie, *Nano Energy* **2015**, *16*, 281.
- [51] M. A. Sadeghi, M. Aghighi, J. Barralet, J. T. Gostick, *Chem. Eng. J. (Amsterdam, Neth.)* **2017**, *330*, 1002.
- [52] J. Gostick, M. Aghighi, J. Hinebaugh, T. Tranter, M. A. Hoeh, H. Day, B. Spellacy, M. H. Sharqawy, A. Bazylak, A. Burns, W. Lehnert, A. Putz, *Comput. Sci. Eng.* **2016**, *18*, 60.
- [53] Q. Xiong, T. G. Baychev, A. P. Jivkov, *J Contam Hydrol* **2016**, *192*, 101.

## Supporting Information

Supporting Information is available from the Wiley Online Library or from the author.

**Acknowledgements**

J.E.B. and G.M. contributed equally to this work. The authors greatly appreciated McGill University's Facility for Electron Microscopy Research for helping us with materials characterization. This work was supported by the Fonds de Recherche du Quebec- Nature et Technologies and the Natural Sciences and Engineering Research Council of Canada Strategic Grant.

Received: ((will be filled in by the editorial staff))

Revised: ((will be filled in by the editorial staff))

Published online: ((will be filled in by the editorial staff))

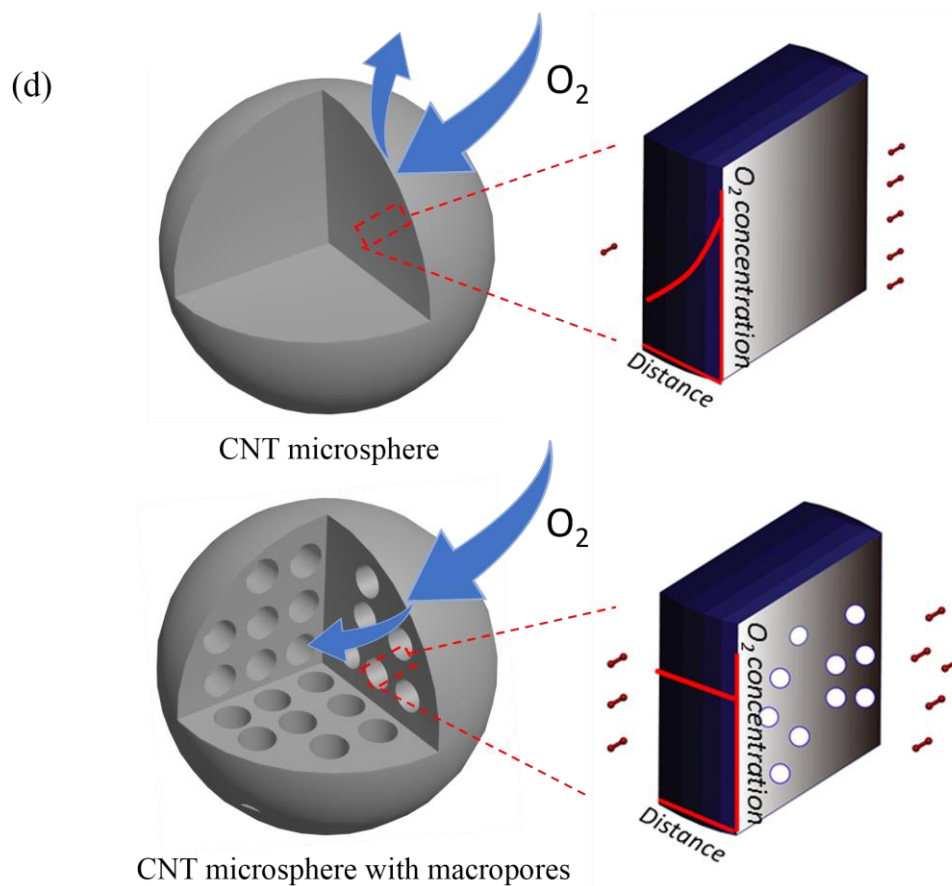
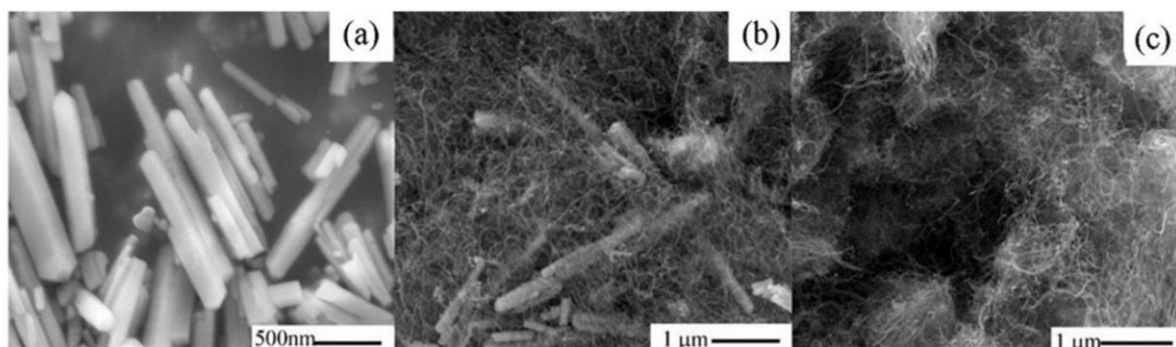


**Figure 1.** SEM images of aragonite (a), aragonite embedded in carbon nanotube microspheres (CN $\mu$ S) (b), and the pore created on the surface of CN $\mu$ S after the removal of porogen (c). Illustration of oxygen diffusion process within CN $\mu$ S with and without macropores, respectively (d).

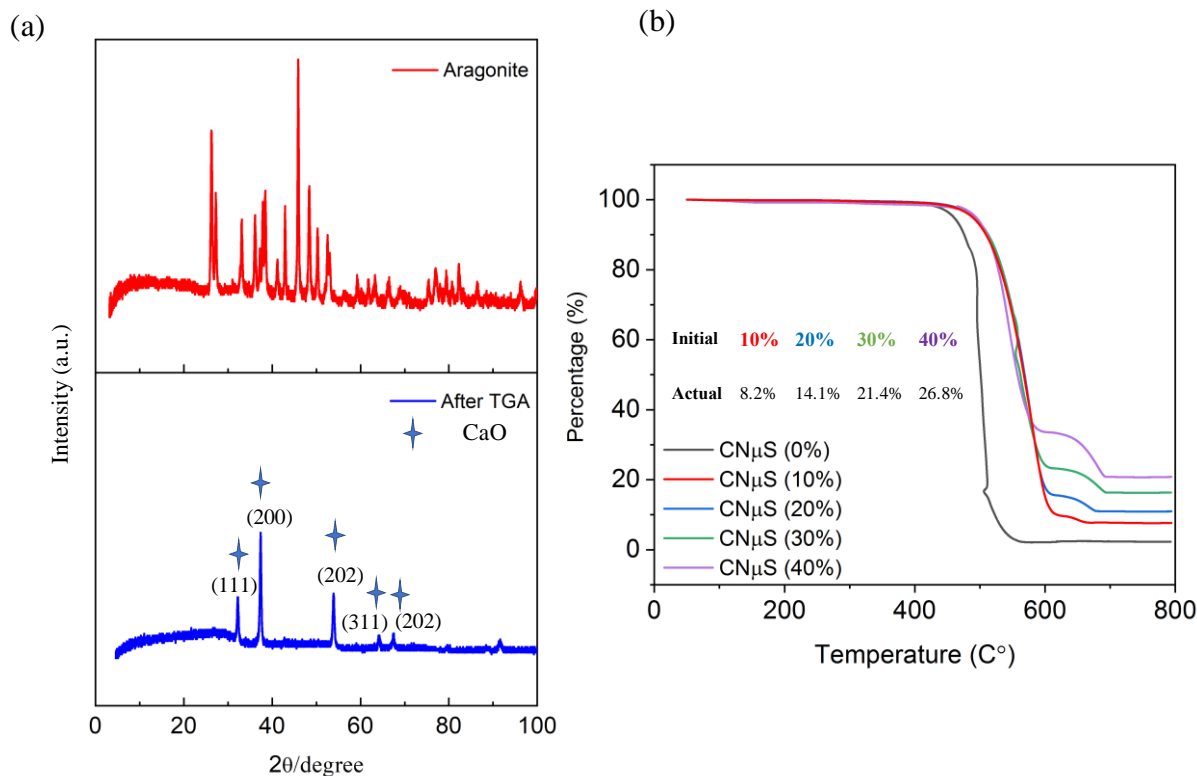


**Figure 2.** XRD patterns and TGA analysis for different CN $\mu$ S-x. XRD patterns for aragonite (a) and the residue (CaO) after the TGA test (800  $^{\circ}\text{C}$ ). TGA curves of different percentage of CN $\mu$ S-x with heating rate 5  $^{\circ}\text{C min}^{-1}$ , and the relationship between starting aragonite percentage ( $W_{\text{ara}}/W_{\text{CN}\mu\text{S}}$ ) and actual aragonite percentage ( $W_{\text{ara}}/W_{\text{CN}\mu\text{S}}$ ) determined by TGA tests ( $\text{CaCO}_3 \rightarrow \text{CaO} + \text{CO}_2$ ) (b).

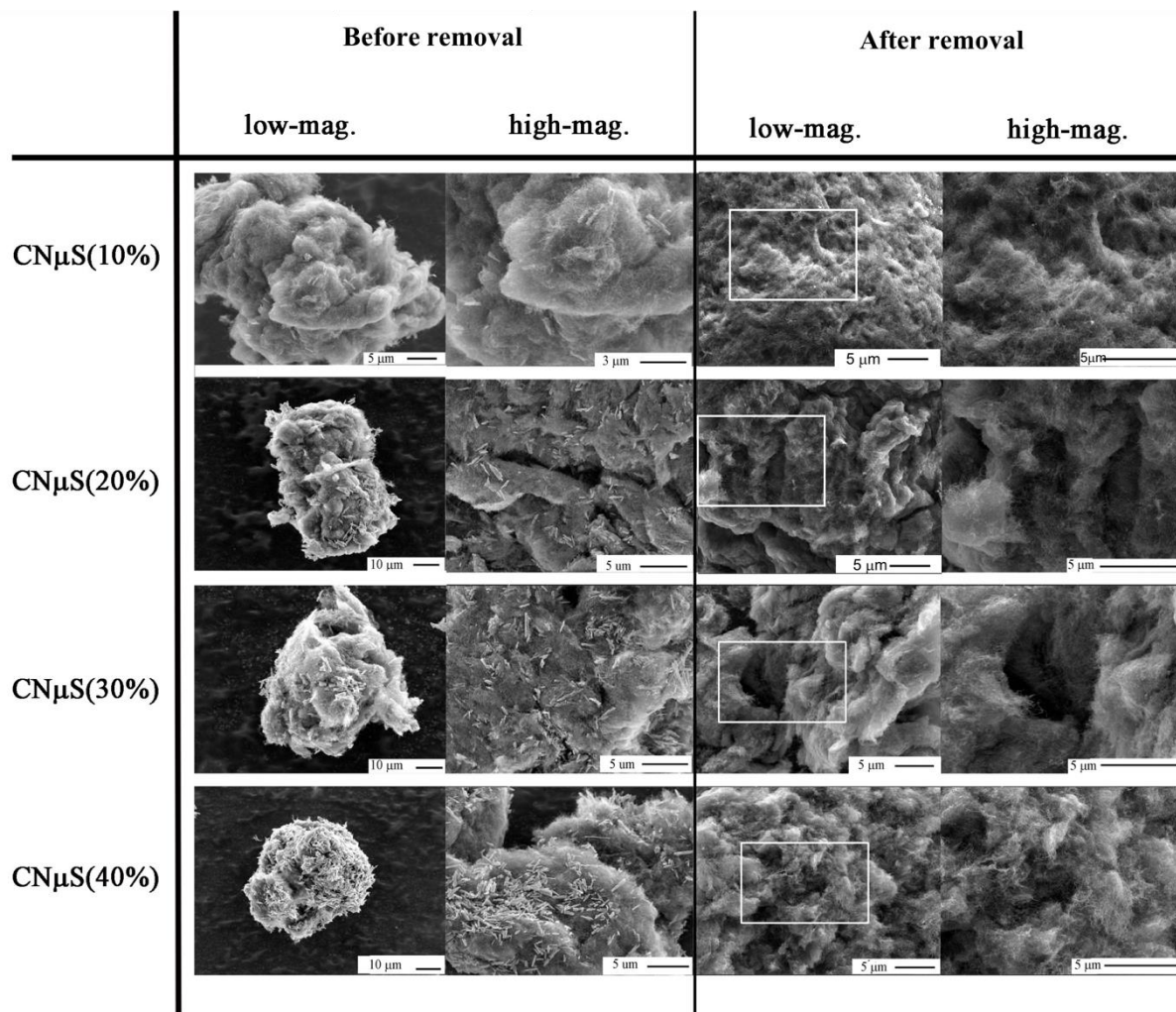


**Figure 3.** SEM images of the surface structures of CN $\mu$ S-x before and after aragonite removal.

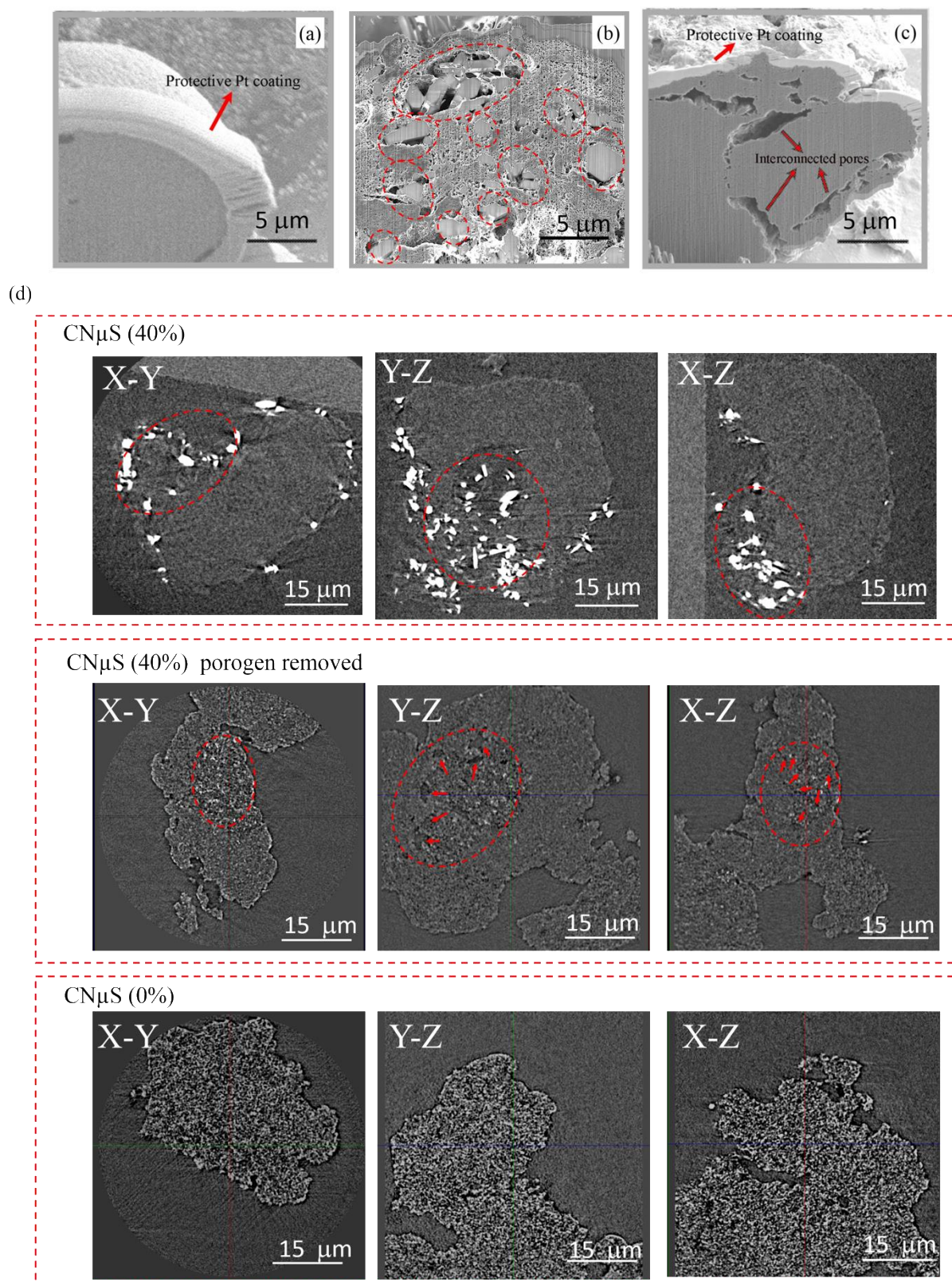


**Figure 4.** Macropore formation process. Focused ion beam (FIB) SEM images of the cross-section of CN $\mu$ S(0%) (a), CN $\mu$ S(40%) (aragonite highlighted in red circles) (b) and the final porous CN $\mu$ S after porogen removal (c). Ultra-CT tomography images of CN $\mu$ S (40%) before and after porogen removal and CN $\mu$ S (0%) (d).

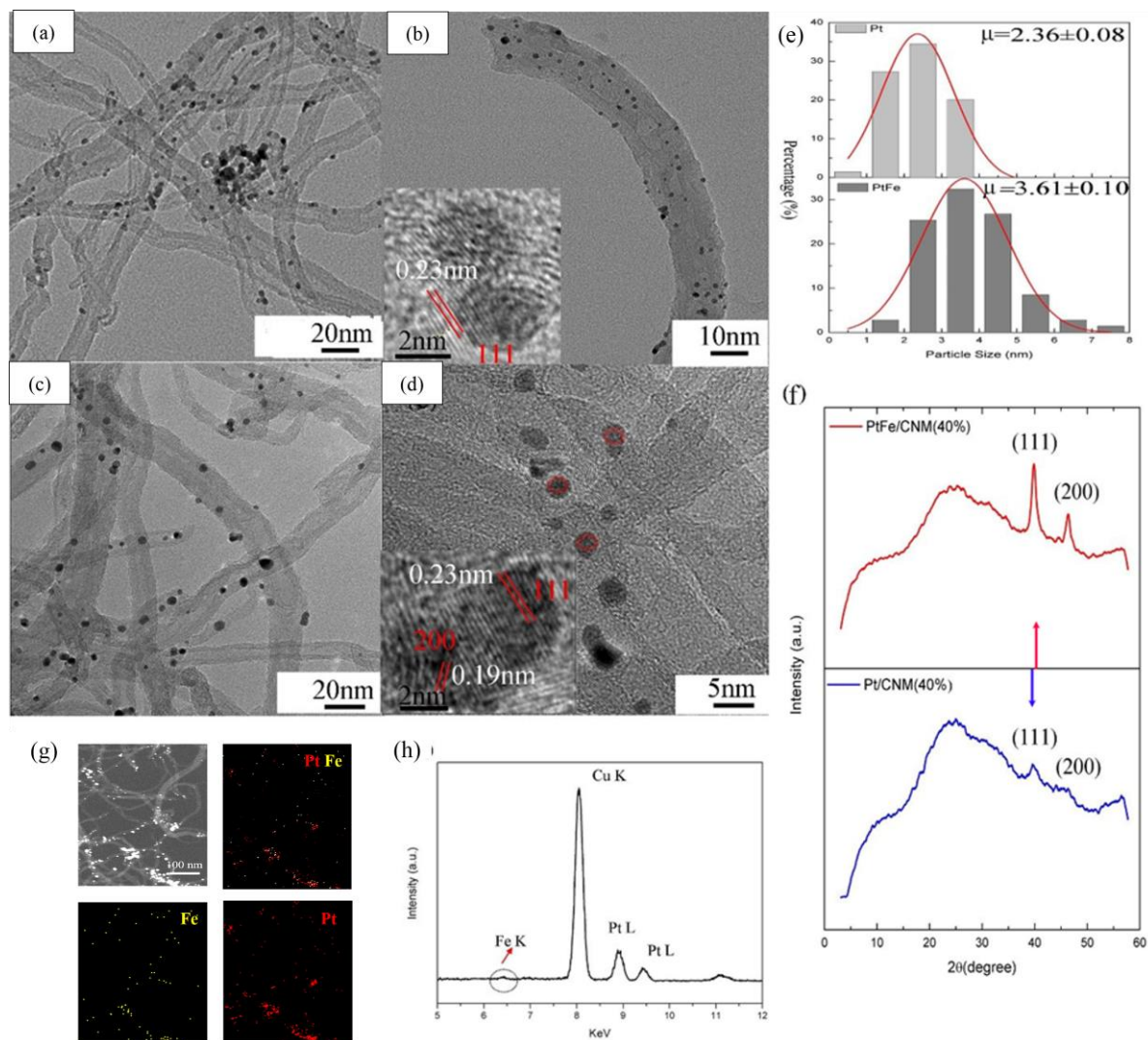


**Figure 5.** Structural formation of Pt and PtFe particles. TEM images of Pt particles (insert b: HRTEM image of Pt particles) (a-b). TEM images of PtFe particles (insert d: HRTEM image of PtFe particles) (c-d). Size distributions of Pt and PtFe particles (e). XRD patterns for Pt and PtFe deposited CN $\mu$ S samples (f). HAADF-STEM image of PtFe particles and elemental maps for overlapped Pt (red) and Fe (yellow) elements, respectively (g). Elemental point analysis result for PtFe particles(h).

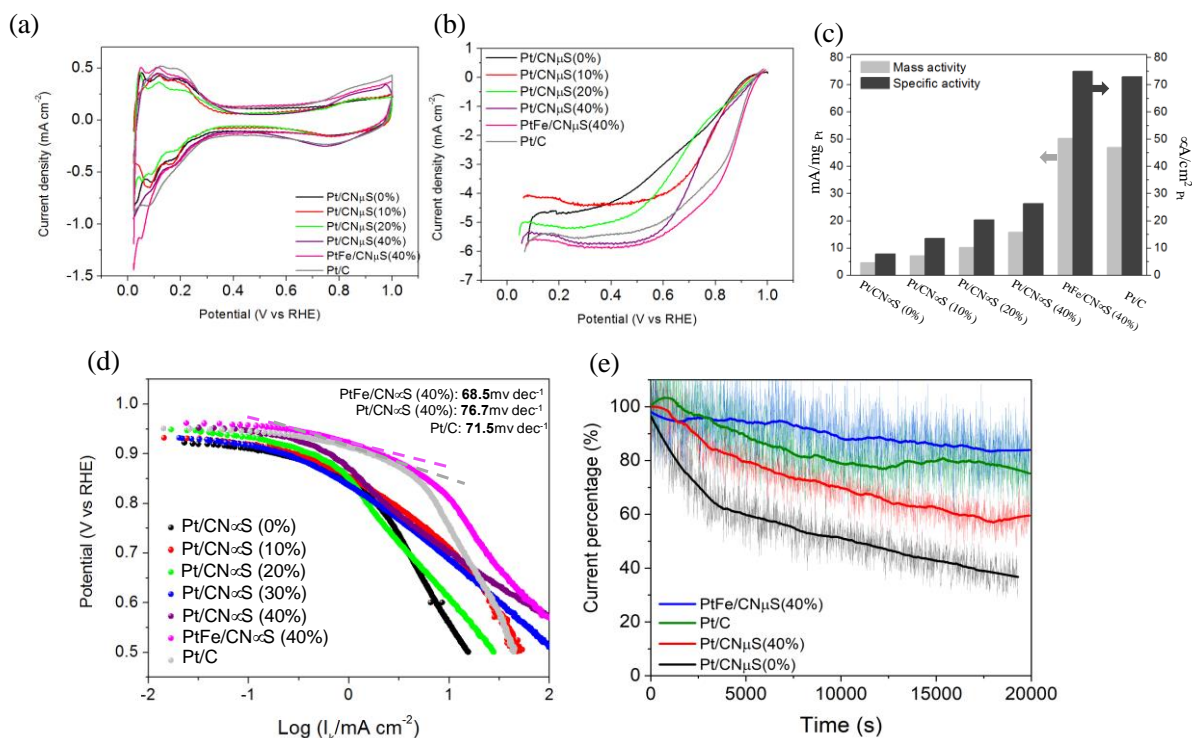


**Figure 6.** Electrochemical characterization. CV curves, LSV curves and comparison of mass and specific activities measured at 0.9 V for different samples (vs. commercial Pt/C) (a-c); Tafel slopes of different percentage CN $\mu$ S based samples (d); Chronoamperometry curves of some selected catalysts obtained at 0.6V (vs RHE) (e); (e). All measurements were performed in 0.1M HClO $_4$  solution, room temperature.

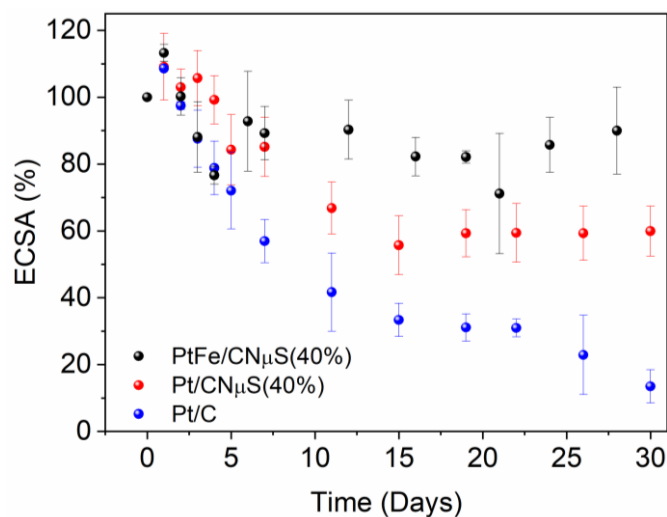


**Figure 7.** Corrosion resistance test. Corrosion resistant performances of different samples were investigated through electrochemical surface area (ECSA) changes for 30 days in 0.1M HClO $_4$  solution.

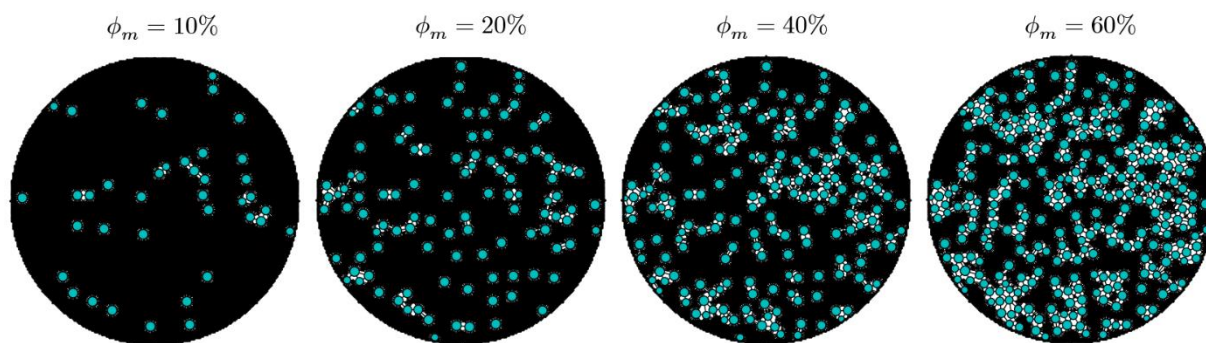


**Figure 8.** Digitally constructed hierarchical particles. Macroporosity progressively increases from left to right. The blue circles are macropores and the black region represents the nanoporous network (nanopores are not distinguishable in the figure because of their high density).

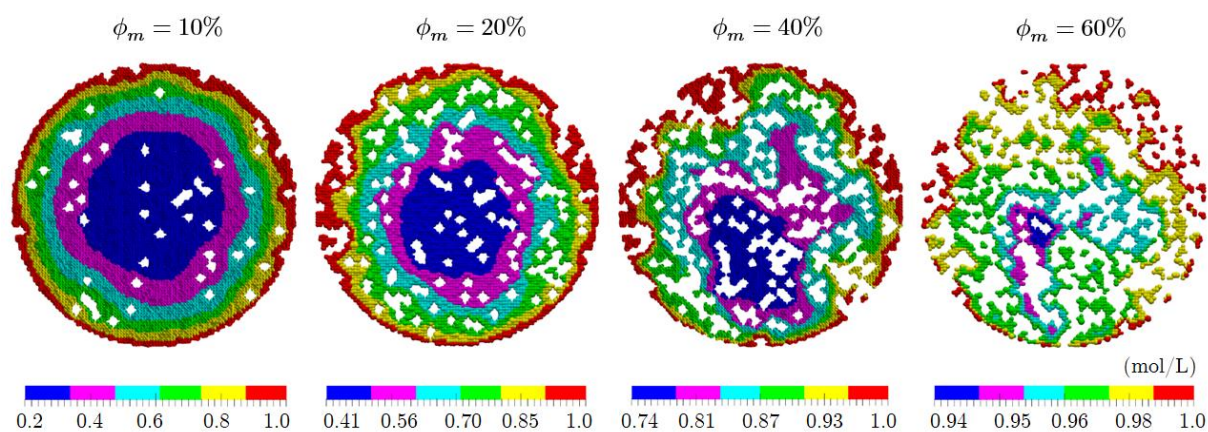


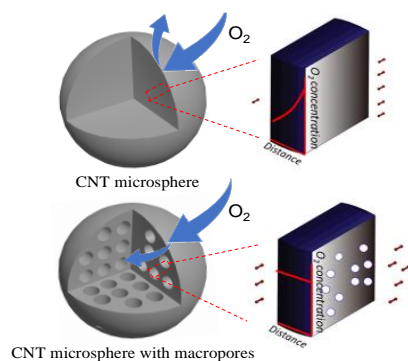
**Figure 9.** Concentration profile within particles with different macroporositities, obtained from the pore network simulation. The colored regions show the nanoporous network and the void space represents the macropores. The particle size is 20  $\mu\text{m}$ .

**3D** micro-structured CNT microspheres can reduce health issues associated with nanoscale materials, and aragonite was employed to tailor the microspheres porosity to decrease micro-size thick diffusion limitations. A significant impact on both surface and inner structures were achieved through this method. PtFe nanoparticles are further deposited to enhance its ORR catalytic activity and optimize Pt usage. Network modeling simulations was conducted showing that starvation blob at the core of microspheres is shrinking with macroporosity increasing, which further confirmed the experimental results.

**Keyword:** carbon nanotube microspheres, porosity, macropores, platinum nanostructures, oxygen reduction reaction

Zishuai Zhang, Mohammad Amin Sadeghi, Siyu Ye, Jeff T. Gostick, Jake E Barralet ‡\* and Geraldine Merle ‡

**Title:** Tailoring carbon nanotube microsphere architectures with controlled porosity



Copyright WILEY-VCH Verlag GmbH & Co. KGaA, 69469 Weinheim, Germany, 2016.

## Supporting Information

### **Title: Tailoring the porosity of carbon nanotube microsphere architectures for fuel cell applications**

*Zishuai Zhang, Mohammad Amin Sadeghi, Siyu Ye, Jeff T. Gostick, Jake E Barralet<sup>†\*</sup> and Geraldine Merle<sup>‡</sup>*

The mass activity and specific activities were calculated based on following equations (Pt loading  $m$  is  $0.04 \text{ mg cm}^{-2}$ ):<sup>[29]</sup>

$$I_m = \frac{I_k}{m} \quad (1)$$

$$I_s = \frac{I_k}{m \times ECSA} \quad (2)$$

### **Particle density measurement:**

For these selected spherical microparticles, the particle densities can be calculated through Stokes' Law:

$$V = 2ga^2(\rho_1 - \rho_2)/9n \quad (3)$$

Where  $V$ = velocity in cm/sec;

$g$ = g force in  $\text{cm/sec}^2$

$\rho_1$ = density of particle in  $\text{g/cm}^3$

$\rho_2$ = density of media in  $\text{g/cm}^3$

$n$ = coefficient of viscosity in poises ( $\text{g/cm-sec}$ )

$a$ = radius of spherical particle in cm

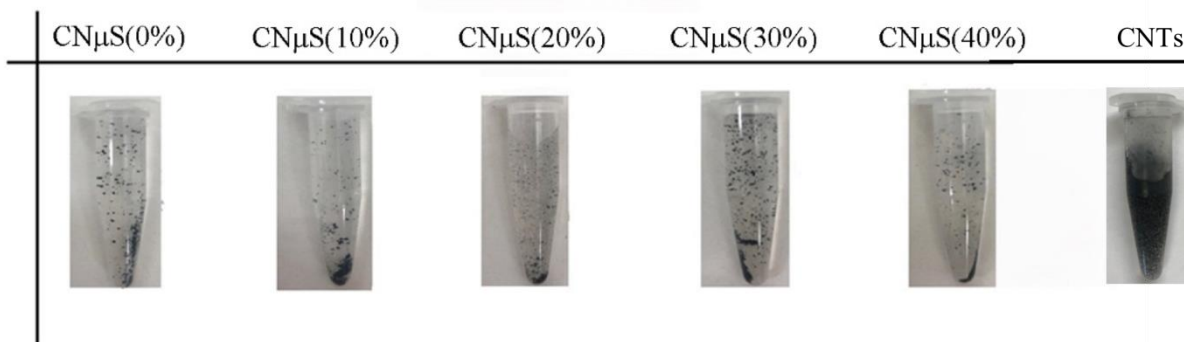


**Figure S1.** Photographs of CN $\mu$ S with different amounts of porogen and CNT control after shaking in a dental amalgamator for 10 s.

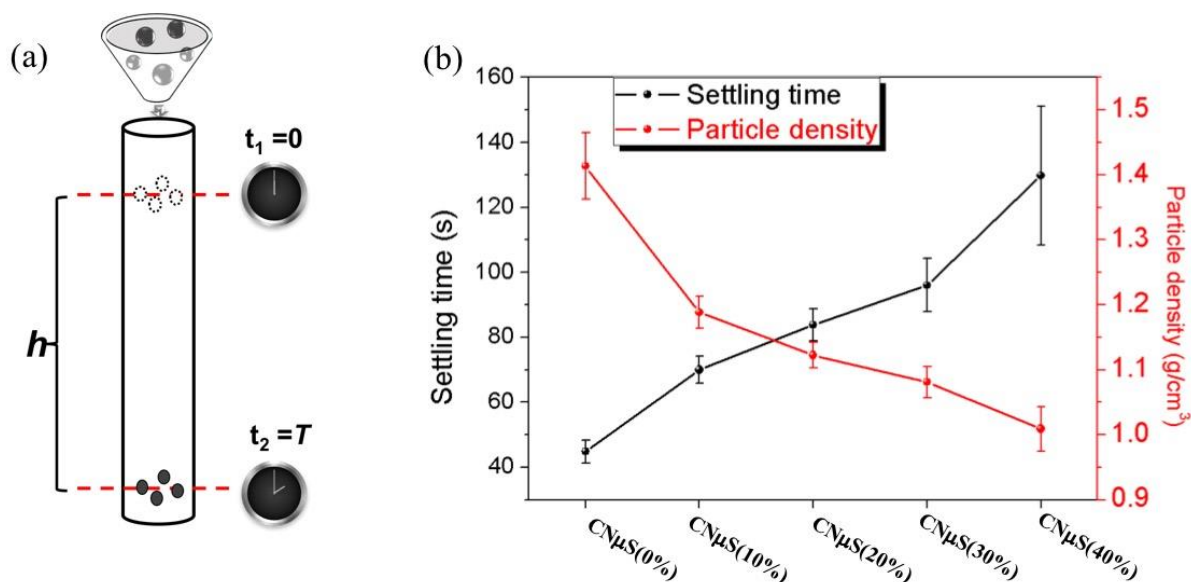


**Figure S2.** Schematic of microparticle density experiment setup (a); settling times and particle densities of various CN $\mu$ S (b).

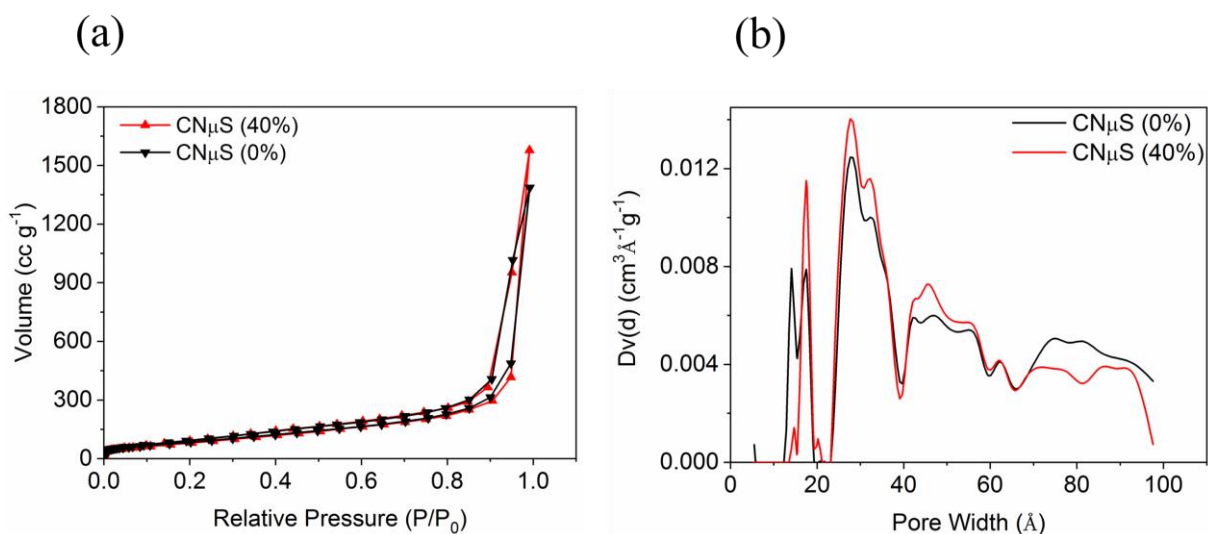


**Figure S3.** Porosity characterization. (a) Nitrogen sorption isotherms. (b) Pore size distributions of CN $\mu$ S (0%) and CN $\mu$ S (40%).

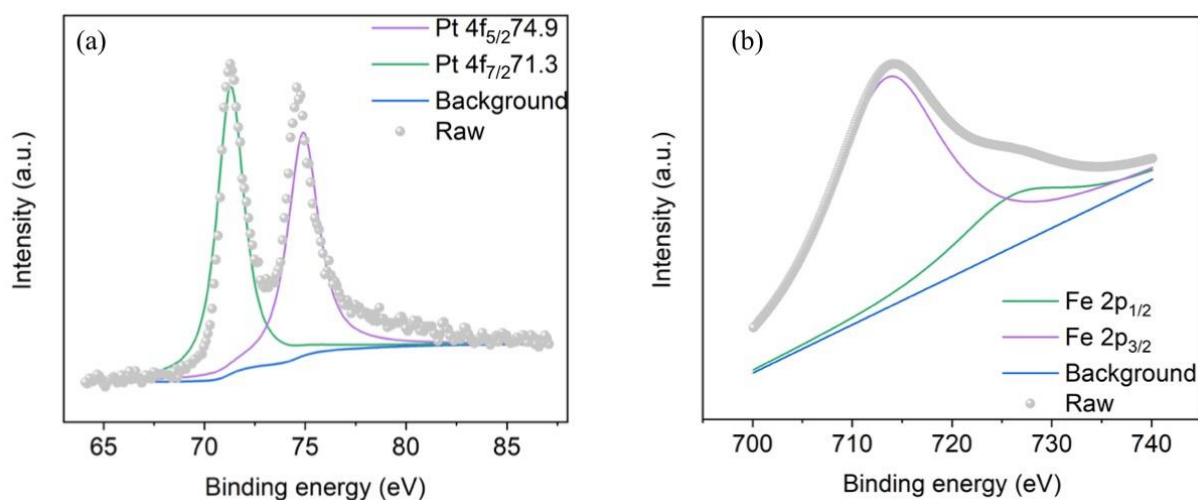


**Figure S4.** High resolution x-ray photoelectron spectroscopy (XPS) of Pt and Fe elements for PtFe/ CN $\mu$ S(40%) .

**Table S1.** Settling times and their corresponding particle densities for various CN $\mu$ S samples.

Supports	CN $\mu$ S (0%)	CN $\mu$ S (10%)	CN $\mu$ S (20%)	CN $\mu$ S (30%)	CN $\mu$ S (40%)
Settle time 1 (s)	46.08	64.55	77.47	107.45	122.92
Settle time 2 (s)	40.06	74.85	84.35	92.08	158.69
Settle time 3 (s)	48.45	70.58	89.55	88.46	107.74
Average settle time (s)	44.86	69.99	83.79	96.00	129.78
Standard dev.	3.53	4.32	4.95	8.23	21.36
particle density (g cm <sup>-3</sup> )	1.41	1.19	1.12	1.08	1.01

**Table S2.** Pt and Fe atomic ratio.

	Initial	EDS (TEM)
Ratio of Pt: Fe (atomic ratio)	1	1.5

**Table S3.** Comparison of electrochemically active surface area (ECSA), mass and specific activities measured at 0.9V for different samples.

Catalysts	Pt/CN $\mu$ S (0%)	Pt/CN $\mu$ S (10%)	Pt/CN $\mu$ S (20%)	Pt/CN $\mu$ S (40%)	PtFe/CN $\mu$ S (40%)	Pt/C
ECSA (m <sup>2</sup> /g <sub>Pt</sub> )	60.2	52.8	50.5	60.1	67.0	64.4
$i_{s(0.9V)}$ ( $\mu$ A/cm <sub>Pt</sub> <sup>2</sup> )	7.8	13.6	20.3	26.4	75.0	72.9
$i_{m(0.9V)}$ (mA/mg <sub>Pt</sub> )	4.7	7.2	10.2	15.8	50.3	47.0